# Interplay of vapor adsorption and liquid imbibition in nanoporous Vycor glass

Sebastian Kiepsch and Rolf Pelster
*Experimental Physics, Saarland University, 66123 Saarbrücken, Germany*
(Received 6 October 2015; revised manuscript received 4 February 2016; published 25 April 2016)

We have studied the kinetics of spontaneous capillary rise and of the concurrent vapor adsorption in nanoporous, monolithic samples of Vycor glass with a mean pore diameter of 7.5 nm. As liquids, we have chosen $n$-alcohols ($n = 4$–10) whose vapor pressures at room temperature range from $p_0 = 965$ Pa down to $p_0 = 0.743$ Pa. Dielectric measurements allow us to achieve spatial selectivity to predefined parts of the porous Vycor glass. In this way, we are able to measure the overall uptake of molecules as well as vapor adsorption from the surroundings in unfilled parts of the pore network, i.e., above the liquid menisci of the rising imbibition front. We show that the latter process is unaltered compared to free adsorption in samples suspended above a liquid reservoir. Only at low vapor pressures, i.e., for long alcohols, vapor adsorption can be neglected and the capillary rise follows the theoretical predictions of the Lucas-Washburn $\sqrt{t}$ law. The more volatile the alcohol, the more important the additional adsorption of molecules becomes. We show that the overall filling process in the pore network is well described by a superposition of the Lucas-Washburn law and the measured vapor adsorption. In addition, the experiments give insight into the vapor diffusion dynamics in the porous matrix.

DOI: 10.1103/PhysRevE.93.043128

## I. INTRODUCTION

The properties of soft matter confined to nanoporous solids are of great interest in current research [1]. Due to self-organizing fabrication processes, many porous materials exhibit homogeneous characteristics over macroscopic length scales. This is beneficial in a variety of technical applications, e.g., as chemical catalyst supports [2,3] or in biotechnology [4]. From an experimental point of view, nanoporous solids provide access to microscopic confinement in a macroscopic sample geometry. In a nanoporous environment, surface forces dominate many physical phenomena, such as capillary flow: When put in contact with a wetting liquid, the pore space fills readily because of predominant capillary forces. The driving force for this flow results from a difference in surface energy between the wetted and unwetted state.

In standard porous media theory, as typical pore sizes are in the range of micrometers, a hydrodynamics approach yields accurate flow rates for spontaneous capillary rise or two-component displacement flows in defined geometries [5], providing a suitable framework for technical applications, e.g., in gas or oil recovery [6]. In contrast to this macroscopic situation, continuum theory and derived fluid parameters cannot be applied *a priori* if typical molecular dimensions are comparable to pore sizes. However, in the mesoscopic range of pore radii $r_0$ from 2 to 50 nm, experimental spontaneous imbibition flow rates are still in good agreement with flow rate predictions from continuum theory and great robustness of macroscopic fluid parameters such as viscosity and surface tension is observed [7,8]. In previous works, deviations from predicted flow rate coefficients were often attributed to microscopic effects. In this context, there are reports of two different phenomena depending on the combination of liquid and matrix. First, slip flow occurs if the molecular layers closest to the pore boundary are not pinned to the matrix, resulting in higher flow rates [9,10]. Second, the opposite case of fixed molecular layers on the wall reduce the hydrodynamic radius of the flow channel and thus the flow rate significantly [11].

Besides the capillary flow, there can be a secondary molecular transport by diffusion and subsequent adsorption from the external vapor phase. In previous studies, this effect was ruled out by either limiting the experiments to liquids that exhibit low vapor pressures or sealing the sample surfaces exposed to the vapor [12]. The latter situation corresponds to the limiting case of a semi-infinite sample only exposed to one-sided imbibition. Of course, we cannot exclude *a priori* the evaporation of the advancing liquid and recondensation farther away and shall discuss this point later on. The opposite limit, pure diffusion and/or adsorption of vapor molecules has also been studied [13–16]. An intermediate regime is to allow maximum vapor transport in a finite sample, combining the effects of one-sided imbibition and vapor adsorption from all free sides in a controlled atmosphere. To our knowledge, such a co-occurrence of both, capillary flow and vapor adsorption, has not been described so far. Hence, it is not clear whether these two transport mechanisms are independent or interact with one another. Does vapor adsorption accelerate the liquid movement inside the pores or does the classical capillary-rise dynamics persist and can be unveiled despite the complexity of the overall dynamics? The goal of this work is thus to take a closer experimental look at the dynamics of the spontaneous imbibition process, especially on the contribution of vapor adsorption during hydrodynamic imbibition flow. For this purpose we use mesoporous Vycor glass (PVG) as a porous host and primary $n$-alcohols (chain lengths $n = 4$–10) as filling liquids. The $n$-alcohols are a class of simple, polar organic molecules. Since the Vycor silica matrix features highly polarized surface bonds, the fluid molecules can potentially interact by strong intermolecular forces, e.g., dipolar forces. Instead of falling back on microbalances—a very common technique to determine the mass increase in imbibitions experiments—we employ dielectric spectroscopy. It features area selectivity and thus provides an insight into the filling dynamics of different parts of the sample. In this way we are able to measure the adsorption kinetics as a single filling mechanism as well as in parallel to liquid imbibition. In the end we shall propose an empirical

 

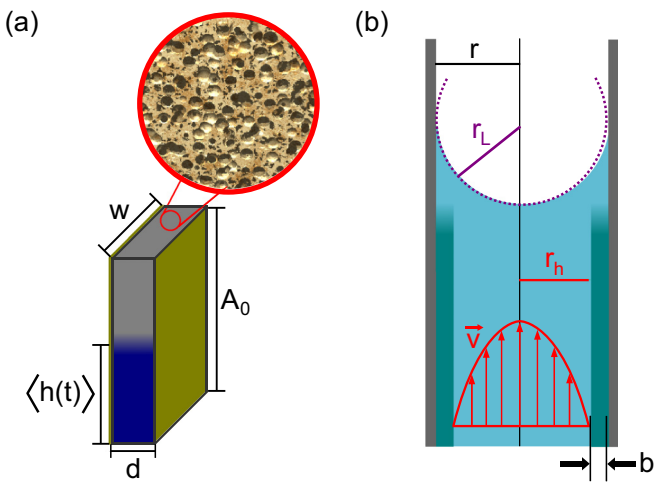


FIG. 1. Sample and pore geometry. (a) Typical nanoporous Vycor sample during an imbibition experiment with imbibition front at position $h(t)$. Vycor has a spongelike microstructure containing a network of interconnected pores, as illustrated in the circular inset. (b) The individual pores feature a cylindrical cross section. When a capillary flow fills the empty pore space, a parabolic velocity profile is expected. Its width $r_h$ depends on a slip boundary condition (see text). Here, the case of $r_h < r$ and $r = r_L$ ($\theta = 0^\circ$) is depicted, which was assumed for $n$-alcohols on Vycor glass.

model that quantifies its impact on apparent capillary flow coefficients.

## II. THEORY

### A. Dynamics of spontaneous capillary flow

When a cylindrical capillary is put into contact with a wetting liquid, concave menisci form inside the capillary [see Fig. 1(b)]. The resulting curvature $r_L$ depends on the contact angle $\theta$ and the capillary radius $r$. A Laplace pressure $p_L$ exerts a force on the liquid surface of surface tension $\sigma$, causing spontaneous rise:

$$p_L = \frac{2\sigma}{r_L}. \tag{1}$$

As the rise height inside the capillary increases, the hydrostatic pressure of the liquid counteracts the Laplace pressure until an equilibrium state is reached. The capillary radius $r$ is inversely proportional to $p_L$ and the maximum height of capillary rise $h_{\max}$ resulting from an equilibrium of hydrostatic and Laplace pressure. For $r$ in the range of a few nanometers, typical values are $p_L > 100$ bar and $h > 1$ km. On the experimental scale in this work, i.e., sample heights in the order of $h_0 \approx 1$ cm [see Fig. 1(a)], the hydrostatic pressure is negligible compared to capillary pressure.

The capillary flow dynamics results from the solution of the Navier-Stokes equations for incompressible fluids. In nanoscale flow channels, the Reynolds number is typically very small and Stokes flow is expected. The liquids used in this work are Newtonian liquids with a dynamic viscosity $\eta$. In cylindrical capillaries, a parabolic flow profile is expected. The maximum velocity is reached along the central axis and it drops to zero at a certain hydrodynamic radius $r_h$ [see Fig. 1(b)]. In macroscopic flows, the no-slip boundary condition $r_h = r$ usually yields accurate flow rate predictions. However, in mesoscopic pores, effects at the pore wall become more important due to the large surface-to-volume ratio. Depending on whether there is slip flow or fixed wall layers, the slip length $b = r_h - r$ can either be positive or negative.

A Hagen-Poiseuille law then defines the volumetric flow rate $\dot{V}(t)$ in a single nanopore, where the channel length equals the current rise height $h(t)$. This flow in turn advances the liquid column height at a velocity $\dot{h}(t) \propto \dot{V}(t)$. The resulting differential equation $\dot{h}h = \text{const}$ can be solved for $h(t)$ by a $\sqrt{t}$ law, which is commonly known as the Lucas-Washburn law [17,18]:

$$h(t) = \sqrt{\frac{\sigma}{2\eta}}\sqrt{\frac{r_h^4}{r_L r^2}}\sqrt{t}. \tag{2}$$

In contrast to single flow channels, Vycor glass contains an isotropic network of interconnected pores of a finite size distribution. This geometric complexity needs to be considered in flow rate equations. In real pore networks, only a part of the total porous volume contributes to flows in any specific direction. Moreover, the pores are rather meandering than perfectly straight. Both of these effects result in an apparent elongation of flow channels in hydrodynamic flow. For this reason a tortuosity factor $\tau$ is introduced in flow rate equations [$\dot{V}(t) \to \frac{1}{\tau}\dot{V}(t)$], resulting in a factor $\frac{1}{\sqrt{\tau}}$ on the right-hand side of Eq. (2). Obviously, $\tau = 1$ is found for a flow along linear pores, as described by Eq. (2). Similarly, in a three-dimensional (3D) lattice of interconnected, straight and perpendicular pores, one expects $\tau = 3$ for flows in parallel to one of the three pore axes, since only every third pore is an effective flow channel. In real isotropic networks, due to complex pore shape, a higher value for $\tau$ is observed. For porous Vycor glass, we have obtained $\tau = 3.6 \pm 0.1$ from self-diffusivity measurements during gas permeation (see [19] for the theoretical background). Regarding the pore size distribution, Eq. (2) can be expressed in terms of the mean pore radius $r_0$ [20] resulting in an averaged rise height $\langle h(t)\rangle$ of the liquid:

$$\langle h(t)\rangle = c_h\sqrt{t} = \sqrt{\frac{\sigma}{2\tau\eta}}\sqrt{\frac{(r_0+b)^4}{r_L r_0^2}}\sqrt{t}. \tag{3}$$

Equation (3) gives no information on the shape of the boundary between filled and unfilled pore space, i.e., the so-called imbibition front. Due to the finite distribution of pore radii, a fluctuation $\Delta h$ in rise height is expected, resulting in a partial filling of the sample for $h \in [\langle h(t)\rangle - \frac{1}{2}\Delta h, \langle h(t)\rangle + \frac{1}{2}\Delta h]$, the so-called imbibition front broadening. In numerical simulations and experiments, $\Delta h$ increases as a function of $\sqrt{t}$ [21–23]. Also, note that Eq. (3) contains no sample parameters, such as porosity or macroscopic geometry, as these are assumed to be independent of $h(t)$.

### B. Vapor adsorption and diffusion in nanopores

In many technical applications, nanoporous compounds, e.g., silica gel, are used to trap molecules from the surrounding gaseous phase. In equilibrium situations at partial pressures $p$

below the bulk vapor pressure $p_0$, two different spatial configurations of adsorbate are reported from sorption isotherm experiments: At low pressures, molecular mono- or multilayers cover the pore walls. These physisorbed molecules, which for Vycor constitute up to 35% of total adsorbate [24], are quite mobile and can rearrange on the surface as well as desorb again. For higher partial pressures above a critical pressure $\tilde{p}$, capillary condensation takes place: The situation of a capillary bridge with concave menisci is energetically favorable compared to adding more layers. According to Kelvin's equation, the radius of curvature of the liquid meniscus $r_c$ is related to the reduced vapor pressure $\tilde{p}/p_0$, depending on the surface tension $\sigma$ and the molar volume $V_m$ of the liquid adsorbate [25]:

$$\frac{\tilde{p}}{p_0} = \exp\left(-\frac{2\sigma V_m}{RTr_c}\right). \tag{4}$$

The meniscus curvature $r_c$ is usually expected to be smaller than the pore radius, since the capillary bridges form on top of the adsorbed multilayers that exhibit some degree of interaction with the pore walls [26]. The contact angle between the capillary bridge and the multilayers is assumed to be $\theta = 0$, as bulklike fluid properties are expected for multilayer systems in the layers farthest form the pore walls. For finite pore size distributions, the transition from multilayers to capillary bridges occurs at different reduced vapor pressures. This allows one in turn to calculate a relative distribution of pore radii (Kelvin radii + multilayer thicknesses for planar substrates) from measured nitrogen sorption isotherms. This method is accurate for pore sizes down to $r_0 = 3.0$ nm [25]. Note that during the capillary flow of alcohols as a nonequilibrium process, the meniscus curvature is not necessarily the same as in sorption isotherms ($r_L \neq r_c$). In particular, as the alcohol molecules are much larger than nitrogen molecules, only a monolayer condensation is expected. We will discuss this in Sec. IV A.

In nonequilibrium, molecules adsorb and desorb with different local rates depending on conditions such as local curvature and coverage of the pore walls, presence of capillary bridges, etc. The consequence is a concentration gradient of vapor molecules driving a diffusion flux according to Fick's first law. Since this flux depends on the filling state of the pores it changes as a function of time. It is worth noting that the concentration gradient is not limited to the pore volume but will extend into the surroundings of the sample. The reason for this is the finite transport diffusivity of the bulk vapor phase consisting of alcohol vapor and helium gas (see Sec. III). The magnitude of this effect strongly depends on the ratio of diffusivities outside and inside the pores. According to Chapman-Enskog theory [27] the diffusivity in the bulk vapor phase can be estimated in first order approximation to an order of magnitude of $D_{\text{bulk}} \sim 1\ \text{mm}^2\,\text{s}^{-1}$. This approximation is independent of the concentration of vapor molecules in the gas phase and thus constant during the adsorption process, while the diffusivity of the pore network undergoes critical changes that we will discuss below. These changes should reflect qualitatively in the overall flux, even for bulk diffusivities comparable to pore diffusivities (i.e., at least as long as the transport in the vapor phase does not govern the total response).

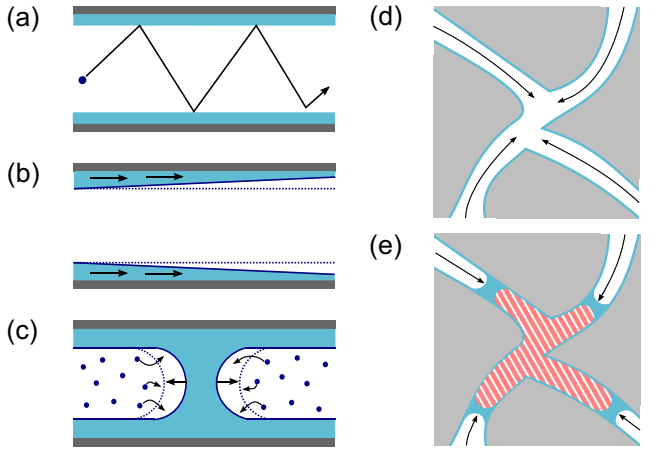


FIG. 2. Transport mechanisms and two-dimensional network topologies during vapor adsorption. (a) The transport of molecules inside the pores is largely determined by a Knudsen diffusion in the gaseous phase. The mean free path of vapor particles is typically larger than geometrical constraints. Interactions with the pore walls then govern the molecular movement as opposed to particle-particle interactions in a bulk gas. (b) Adsorbed layers at the pore walls partially retain their mobility. They directly contribute to molecular transport by surface diffusion. (c) Capillary bridges inside the pores provide additional adsorption spots for vapor molecules. Condensation on capillary bridges enables a hydrodynamic advancement of the concave menisci, while disabling Knudsen diffusion along this pore. (d) The network topology gradually changes during the adsorption process. For low pore loadings, adsorption is limited to molecular layers. (e) At higher pore loadings, capillary bridges obstruct the vapor transport inside the pores and parts of the pore volume may have no connection to the bulk vapor.

We will put this to the test in adsorption kinetics experiments (see Sec. IV B).

Figures 2(a) and 2(b) illustrate the different mechanisms of molecular transport during adsorption. Diffusion inside the empty pore space is largely determined by a Knudsen mechanism [14,15], as the mean free paths of vapor molecules are typically larger than geometrical constraints. For empty pores, Knudsen diffusivities $D_{\text{Kn}} \approx 0.14$ to $0.2\ \text{mm}^2\,\text{s}^{-1}$ can be calculated for decreasing chain lengths of the alcohol (C10 to C4), as described in [15]. This value is smaller than that of the bulk diffusivity, confirming that molecular transport in the pores should indeed be visible in the measured adsorption dynamics. During the condensation of molecular wall layers, a decrease of the Knudsen diffusivity $D_{\text{Kn}}$ in accordance to the decrease in pore radius is expected. In addition, surface diffusion in the adsorbed layers contributes to the total diffusion flux, which becomes more important for increased pore loadings in the multilayer domain [16,28]. When capillary condensation starts, those capillary bridges that can be reached from the outside act as additional diffusion sinks [see Fig. 2(c)]. When vapor molecules condense here, the capillary bridge increases in size. Note that the meniscus curvature and thus the local vapor pressure remain constant in the process. Moreover, capillary bridges effectively seal the respective pores for vapor transport. Depending on the distribution of capillary bridges, parts of the pore network can

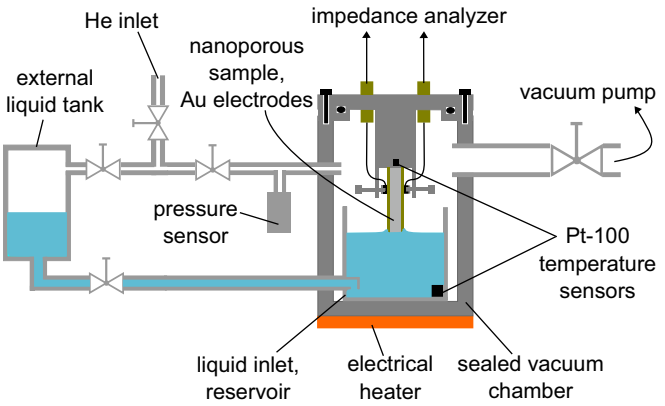


FIG. 3. Schematic of the experimental setup used in this work. It consists primarily of a sealed chamber containing a liquid reservoir and a suspended nanoporous sample. Liquid level and atmosphere can be controlled externally. Both imbibition dynamics and vapor adsorption dynamics can be measured, depending on the amount of liquid inserted. Here, the case of an imbibition experiment is depicted, as the sample touches the liquid surface. The rising liquid inside the porous matrix is detected by means of dielectric spectroscopy.

be cut off from the outside vapor phase [see Fig. 2(e)]. Due to these alterations in the pore network, the overall diffusivity during capillary condensation is reduced significantly [29]. In this situation, the primary filling mechanism is hydrodynamic flow: A pressure difference that is caused by a difference in meniscus curvature on both sides of a capillary bridge, e.g., because of the pore size distribution, results in an effective flow of liquid.

In conclusion, during the filling process, the diffusion mechanism, the concentration gradients of the vapor molecules, and the topology of the partially filled pore network change. As a consequence, adsorption dynamics is rather complex. In contrast to liquid capillary flow that is well described by Eq. (3), there is no simple analytical solution for vapor adsorption dynamics.

## III. EXPERIMENTAL METHODS

The measuring method presented in this work is an approach to quantify liquid filling in a porous matrix using dielectric measurements (see Fig. 3). The porous samples are kept in a sealed chamber with controllable atmosphere (He + adsorbate). On one hand, the sealed chamber prevents outside contaminants from reaching the sample; especially water vapor can produce a significant signal when adsorbed in the pore space, because of its high static permittivity ($\varepsilon_{\text{stat}} \approx 80$). On the other hand, this guarantees reproducible adsorption kinetics: In previous works under ambient conditions [30], the partial pressure of vapor is expected to be smaller than the bulk vapor pressure ($p < p_0$) due to diffusion into the surrounding air as an infinite sink. While this reduces the contribution from vapor adsorption to total sample filling, the adsorption then critically depends on changing external conditions. This adds an uncertainty to the overall filling dynamics. In contrast to this situation, a saturated vapor atmosphere ($p = p_0$) is expected in the above setup if no sample is present. Since this pressure

TABLE I. Vapor pressures $p_0$, viscosities $\eta$, and surface tensions $\sigma$ of $n$-alcohols ($T = 293$ K), values taken from [36–38].

| Name | $n$ | $p_0$ (Pa) | $\eta$ (mPa s) | $\sigma$ (mN m$^{-1}$) |
|---|---|---|---|---|
| Butanol | 4 | 965 | 2.81 | 24.3 |
| Pentanol | 5 | 208 | 3.97 | 25.1 |
| Hexanol | 6 | 77.1 | 5.21 | 26.1 |
| Heptanol | 7 | 22.54 | 6.83 | 26.6 |
| Octanol | 8 | 7.46 | 8.78 | 27.3 |
| Nonanol | 9 | 2.52 | 10.85 | 28.2 |
| Decanol | 10 | 0.743 | 14.06 | 28.8 |

highly varies between the different alcohols (see Table I), an additional helium filling of a defined pressure $p_{\text{He}} = 800$ mbar is added. The high value for $p_{\text{He}}$ was chosen in order to recreate the ambient pressure of previous experiments as close as possible without breaking the seal.

If a sample is present in the chamber, adsorption of vapor molecules in the pores is expected, while helium condensation can be ruled out at room temperature. Then, a concentration gradient of alcohol molecules will arise in the bulk vapor phase, which depends on the intermolecular diffusivity in the gas mixture. Inside the pores, because of the predominant Knudsen mechanism, only a small decrease in diffusivity (5% to 10%) is expected because of the increase in pressure [31].

The nanoporous samples are prepared from porous VYCOR 7930 glass (PVG) rods, a now discontinued product of Corning Incorporated [32]. PVG is a monolithic silica glass matrix surrounding an isotropic 3D network of meandering pores of nearly circular cross section. The average volume porosity of PVG is $\Phi \approx 28\%$ which was determined by sorption isotherm measurements. As described in Sec. II B, a mean pore radius of $r_0 = 3.75 \pm 0.15$ nm could be deduced. Like every nanoporous material, PVG is prone to adsorption of molecules from its surroundings, which first need to be removed. The cleaning process, which is described in detail in [32], also applies to imbibed alcohol after an experiment and thus allows multiple uses of the same sample. The typical cuboid sample geometry is depicted in Fig. 1(a), with sample dimensions of approximately 2 mm × 10 mm × 10 mm ($d \times w \times h_0$). After cutting, cleaning, and drying, gold electrodes are applied to the samples by means of physical vapor deposition. The electrodes can be tailored to cover a certain area on the sample by selective masking. For imbibition experiments, the entirety of the flat sides is coated with electrode material, as shown in Fig. 1(a). The electrodes still exhibit a large degree of porosity and do not obstruct the flow of liquid or gas into the sample. We conclude this from preliminary experiments, in which we attempted to forcefully seal the sample by sputter coating, which resulted in unchanged experimental results.

Prior to every measurement, a vacuum of $p_{\text{vac}} \approx 10^{-6}$ mbar is applied to the sample inside the sealed chamber at elevated temperatures $T \approx 343$ K for at least 12 h, evaporating most preadsorbed water and other volatile adsorbates from the porous matrix. However, there is still very likely at least one strongly confined monolayer of water present at all times, whose removal would require even higher temperatures [33]. When the system reaches thermal equilibrium, the controlled

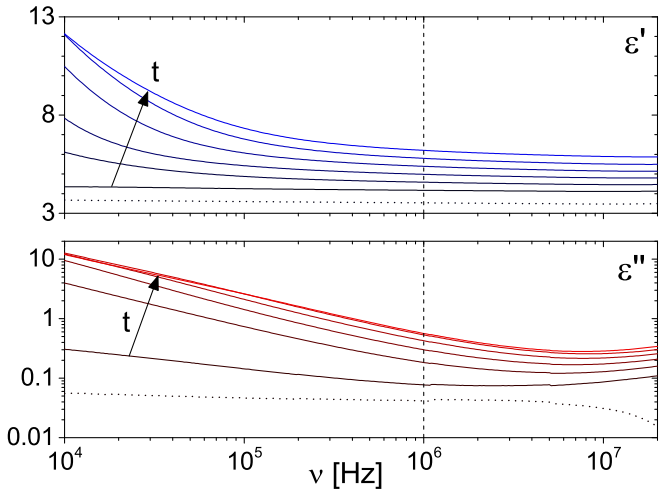


FIG. 4. Dielectric spectra of 1-decanol confined to porous Vycor glass over the course of an experiment: (top) real part and (bottom) imaginary part of permittivity. The dotted lines show the spectra of the empty sample surrounded by air; the continuous lines show the increase in filling ($f = 0\%,20\%,40\%,60\%,80\%,100\%$) over time for a sample in contact with the liquid surface.

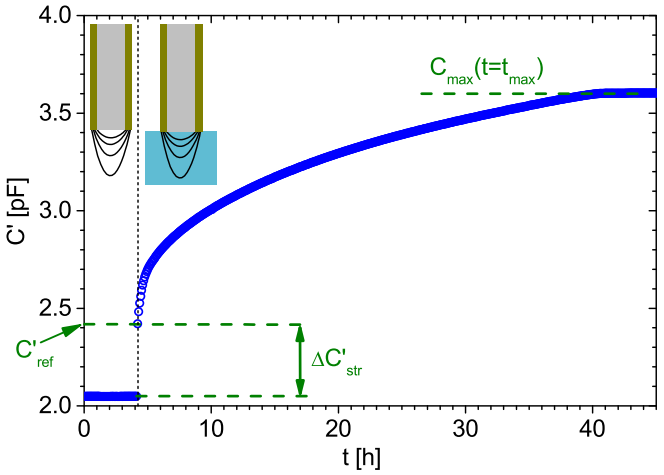


FIG. 5. Evolution of the real part of the total sample capacitance over the course of a typical imbibition experiment, here for 1-decanol. Note the sudden increase at $t = 4$ h due to bulk liquid reaching the stray field when liquid is inserted. The maximum capacity $C_{\max}$ is reached when the sample is entirely filled.

atmosphere and the liquid are inserted into the reservoir from a pressurized outside source and the dielectric measurement is started at a well-defined time.

The dielectric measurements are performed using an Agilent 4294A impedance analyzer which measures the real and imaginary parts of the complex capacitance $C^*(t)$ for a set frequency range of $\nu = 1$ kHz to 20 MHz at fixed time intervals. Changes in $C^*(t)$ correspond to changes in the dielectric function $\varepsilon^* = \varepsilon' - i\varepsilon''$, since the geometric capacitance,

$$C_0 = \epsilon_0 \frac{h_0 w}{d}, \tag{5}$$

remains constant. Here, $h_0$, $w$, and $d$ denote the sample height, width, and depth, respectively [see Fig. 1(a)], and $\varepsilon_0$ is the vacuum permittivity. Dividing the real and imaginary parts of $C^*$ by $C_0$ yields the dielectric spectra, i.e., the real ($\varepsilon'$) and imaginary ($\varepsilon''$) parts of the complex permittivity. The effects of stray capacitance are discussed below.

Typical dielectric spectra are displayed in Fig. 4. In the low frequency domain below 100 kHz, the finite ionic conductivity of the liquid leads to an increase of $\varepsilon''$. The ionic impurities entrapped at the solid-liquid interface also induce an additional polarization and thus an increase of $\varepsilon'$ with decreasing frequency [34]. In addition to these low frequency effects, the dipole relaxation frequency of the longest used alcohol molecules is found just above the measurement range at room temperature [35]. This can be seen for decanol at frequencies $> 5$ MHz in $\varepsilon''$ (see Fig. 4). In order to avoid both of these effects, a fixed frequency of $\nu = 1$ MHz is used for imbibition dynamics analysis. Furthermore, the change in $\varepsilon'$ and $\varepsilon''$ over time differs considerably. Since dipole relaxation losses of the liquid are minimal, the dielectric losses in $\varepsilon''$ depend critically on the role of contaminants, while $\varepsilon'$ reflects the total polarization due to dipolar reorientation. Therefore, $\varepsilon'$ or the real part of the capacitance $C'(t)$ are better suited to quantify the pore loading and will be used from now on.

The spectra in Fig. 4 contain inherent stray field effects that need to be addressed. Most experimental studies on liquid imbibition show a good agreement to Lucas-Washburn dynamics [20]. Accordingly, let us assume at first that vapor adsorption can be neglected and only capillary rise dynamics govern the filling process. As long as the imbibition front is sufficiently flat and front broadening is negligible [see Fig. 1(a)], the normalized filling $f(t)$ follows Lucas-Washburn dynamics, according to

$$f(t) = \frac{V_{\text{liquid}}}{V_{\text{pores}}} = \frac{h(t)}{h_0} \in [0,1]. \tag{6}$$

Then, the sample capacitance $C(t)$ can be modeled as a parallel circuit of three partial capacitances: $C_{V+L}$ for the part that is already filled with liquid, $C_V$ for the part that contains no liquid, and the stray capacitance $C_{\text{str}}$. Both $C_{V+L}$ and $C_V$ change only as a function of the current filling fraction $f(t)$ and the constant permittivities of the full and empty sample, i.e., $C_{V+L} = f(t)\,C_{\text{filled}}$, $C_V = [1 - f(t)]C_{\text{empty}}$. The stray capacitance, on the other hand, is independent of $f(t)$, though a major shift of $C_{\text{str}}$ is expected on liquid insertion, as bulk liquid enters the stray field and external menisci form on the sides of the sample in the vicinity of the bulk liquid interface [see Fig. 6(c)]. As can be seen in Fig. 5, the difference in capacitance $\Delta C_{\text{str}}$ at time $t = t_0$ cannot be measured separately, since the imbibition process starts immediately after the sample touches the liquid. However, $C_{\text{str}}(t)$ is expected to be constant, if both the height of adhering liquid menisci and the level of liquid inside the reservoir do not change significantly during the experiment. We observed neither a time evolution of meniscus height besides the initial snap-in nor any measurable drop of liquid in the reservoir due to evaporation for any of the alcohols. Then, using the first data point after $t_0$ as a reference value for zero filling, $C_{\text{ref}} \approx C_{\text{empty}}$, any difference $\Delta C(t) = C(t) - C_{\text{ref}}$ is free from stray field

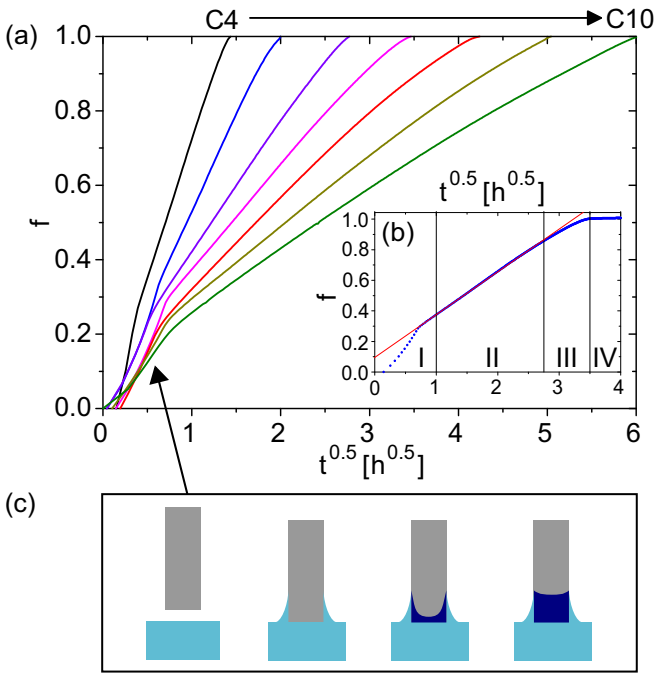


FIG. 6. Experimental data on imbibition of $n$-alcohols ($n = 4$–10) in Vycor. (a) Filling fractions in imbibition experiments plotted over the square root of time. As viscosity increases for higher chain lengths, imbibition dynamics are slower. (b) Typical imbibition experiment, here for heptanol (C7), showing four characteristic segments: (I) initial phase with systematic deviations from Lucas-Washburn dynamics, (II) linear segment with fit, (III) broadened imbibition front reaches the top of the sample, and (IV) pore space is filled entirely. (c) Visualization of time-dependent imbibition front shape because of adhering bulk liquid menisci. During the first experimental phase (I), an additional liquid influx is expected.

effects. When normalized to its maximum value, $\Delta C(t)$ is a measure of relative pore filling:

$$f(t) = \frac{\Delta C(t)}{C_{\max} - C_{\mathrm{ref}}}. \tag{7}$$

An equivalent form is given by the normalized difference in permittivity:

$$f(t) = \frac{\Delta \varepsilon'(t)}{\Delta \varepsilon'_{\max}}. \tag{8}$$

## IV. RESULTS AND DISCUSSION

### A. Experimental imbibition dynamics

Spontaneous imbibition has been measured by means of dielectric spectroscopy for the series of $n$-alcohols $n = 4$–10 [see Fig. 6(a)]. The shorter the chain length of the molecule, i.e., the smaller the viscosity (see Table I), the faster the sample fills. When plotted as a function of $\sqrt{t}$, as depicted in Fig. 6(b), the measured values for $f$ show a good linearity for a large period of time (phase II), corresponding to a height difference of $\approx h_0/2$. There are significant deviations in the beginning (phase I) and at the end (phase III) of the experiments.

As for phase (III), the slower filling over time can be explained by microstructural front broadening, as described in Sec. II A. While Eq. (3) describes the mean filling height, some filled regions are found at a greater height as well as empty regions at lower heights. The partially filled zone, which has macroscopic extent, is observable by eye in experiments due to its different optical properties [22]. At a certain time, the broadened imbibition front reaches the upper sample bound and the overall dynamics slow down, resulting in a negative curvature of $f(t)$. Furthermore, this part of incomplete filling has been neglected in the equivalent circuit for the sample capacitance. This leads to an early onset of phase (III) compared to gravimetric experiments [39].

In order to explain phase (I) of the measurement, one has to consider liquid entering the pores from more than one face of the sample, which can be attributed to the adhering external liquid menisci [see Fig. 6(c)]. Because of this parasitic effect, the imbibition front exhibits a predefined curvature that depends on macroscopic sample and bulk meniscus shape. In order to quantify this multiface imbibition, which should not be confused with front broadening, numerical simulations have been conducted. The results, which will be presented elsewhere, show a good agreement both in magnitude and duration of these deviations. Furthermore, the temporary addition to liquid filling does not critically influence the experiment afterwards. In particular, the front shape flattens over time after the mean rise height passes the external meniscus height $h_{\mathrm{Men}}$.

In summary, the capacitance-in-parallel model and thus Eq. (7) is a valid approximation for phase (II), as long as the macroscopic front shape is sufficiently flat and the extent of front broadening is negligible ($\Delta h \ll h_0$). The total sample capacitance in phase (II) is then expected to feature dynamics $\propto \sqrt{t}$ while exhibiting a $y$ intersect $\neq 0$ in a linear fit. If capillary flow is assumed as the only filling mechanism, $f(t)$ corresponds to the normalized mean height of the imbibition front [see Eq. (6)]. As for phase (II), the slope in $f(t)$ determines the Lucas-Washburn prefactor $c_h$ from Eq. (3):

$$c_h = h_0 \frac{\Delta f(t)}{\Delta \sqrt{t}}. \tag{9}$$

The coefficients $c_h$ for different $n$-alcohols are depicted as circles in Fig. 7. Especially for short alcohols, we observe deviations from what we expect according to the Lucas-Washburn theory. The experimental error in $c_h$ can be estimated by uncertainties in time resolution (difference in time between first contact with the liquid and the first data point at $\nu = 1$ MHz) and thus in the reference value $C_{\mathrm{ref}}$. Additionally, an alternative data analysis can be performed by plotting $f^2(t)$ as a function of $t$. Considering the additional filling from external menisci in phase (I), a constant $f_1$ is assumed after a certain time $t_1$, resulting in

$$f^2(t) = f_1^2 + \frac{\tilde{c}_h^2}{h_0^2}(t - t_1). \tag{10}$$

An order of magnitude of $f_1 \approx 0.1$ is found for all experiments that is consistent with observed heights of external liquid menisci ($h_{\mathrm{Men}} \approx 1$ mm). Note that Eqs. (9) and (10) are not equivalent, thus the parameters $c_h$ and $\tilde{c}_h$ could differ considerably. In our experiments, however, a maximum discrepancy of $\approx \pm 10\%$ was found, which is incorporated in

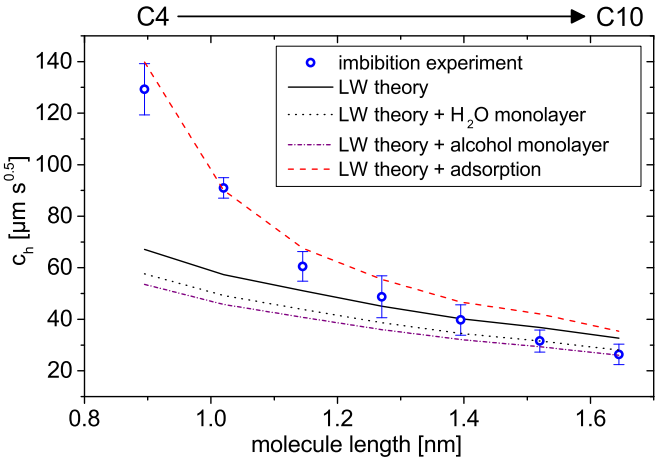


FIG. 7. Experimental Lucas-Washburn coefficients for $n$-alcohols, $n = 4$–10 (○) from imbibition experiments compared to theoretical predictions for a no-slip boundary condition (continuous line), with an immobilized molecular layer of water (slip length $b = -0.275$ nm; dotted line) and with an alcohol monolayer oriented in parallel to the pore wall ($b_{\mathrm{Cn}} = -0.4$ nm; dash-dotted line). Note the increasing deviation of $c_h$ for small $n$, i.e., increasing volatility of the liquid. The theoretical values were corrected for vapor adsorption assuming $b = 0$ (see Sec. IV C). Then, the resulting corrected Lucas-Washburn prefactors (dashed line) explain the upwards deviations of $c_h$ for small chain lengths. (All lines are linear interpolations of data points calculated for the given molecule lengths.)

the error bars in Fig. 7. Hence, the following interpretation is valid for both models, Eqs. (9) and (10).

If we assume total wetting of the pores ($r_L = r_0$), a no-slip boundary condition ($r_h = r_0$) and macroscopic fluid parameters (see Table I), a theoretical value for $c_h$ can be calculated using Eq. (3) (see the continuous line in Fig. 7). A good agreement of experiment and theory can be noted for medium chain lengths $n = 7$–8. For higher numbers of carbon atoms, the measured slopes are lower than expected and vice versa, with higher discrepancies for short chain lengths.

Lower experimental values of $c_h$ have many possible explanations, one of them being immobilized wall layers reducing the hydrodynamic radius. Assuming a slip boundary condition ($r_h = r_0 + b$) and total wetting of the pores with no preceding fluid layers ($r_L = r_0$) in Eq. (3), the experimental values for $c_h$ of the long-chain molecules ($n = 9$ and 10) yield negative slip lengths of $b_9 = -0.28$ nm and $b_{10} = -0.38$ nm. Both values are comparable to the thickness of a molecular layer adhering to the pore walls, which can be estimated from bond lengths and van der Waals radii. From sample preparation, we expect a residual monolayer of water, thus a dotted line in Fig. 7 indicates the expected $c_h$ values for the modified boundary condition ($b_{\mathrm{H_2O}} = -0.275$ nm). Another possibility is a monolayer of alcohol, which—depending on the molecular orientation—causes slip lengths from $b_{\mathrm{Cn}} = -0.4$ nm for orientation in parallel to the pore axis up to the negative molecule length if oriented perpendicularly to the pore wall. The first case is depicted as a dash-dotted line in Fig. 7. For both water and alcohol wall layers, the modified $c_h$ show agreement to experimental results for long-chain alcohols within the error margin. It should also be noted that the choice of boundary condition for $r_L$ and the contact angle $\theta$ result in different slip lengths and thus slightly different values for $c_h$. Another consideration from microscopic lattice model simulations is that the width of the pore size distribution reduces the apparent $c_h$ [40]. While it is remarkable that a continuum description such as Eq. (3) is still appropriate on the pore scale, it is not suited to gain exact information on flow parameters and microscopic behavior in an experiment. Here, a multiscale modeling approach might be useful to determine the slip or no-slip boundary condition at the pore walls [41].

### B. Experimental vapor adsorption dynamics

An upwards deviation of $c_h$ that was found for $n = 4$–6 in Fig. 7 requires an additional flow contribution. Vapor adsorption is a likely process, since the vapor pressure of $n$-alcohols increases by orders of magnitude towards shorter chain lengths (see Table I). In order to quantify the additional diffusion flux from the gas phase, the "concurrent" adsorption during imbibition needs to be separated from capillary flow. Contrary to gravimetric methods, dielectric spectroscopy allows selective measurement on a specific part of the sample. Here, electrodes were placed in an area of height $h_{\mathrm{el}} \approx 0.5h_0$ starting from the top of the sample, and the bottom was left blank, as sketched in Figs. 8(f)–8(g).

For an isotropic network of interconnected pores at porosities $\Phi > 25\%$, such as PVG, the measured permittivity is in a good approximation a linear function of the pore space permittivity $\varepsilon_{\mathrm{pore}}$ [42]. Thus, we expect Eq. (8) to be a fairly good approximation of the filling fraction if the adsorption is homogeneous in the sample volume (and is the only filling mechanism; see below). It has to be noted that the sample geometry, especially the thickness $d$, is expected to change adsorption dynamics critically. Therefore, all following experiments were performed on the same sample, which required a thorough cleaning procedure (see Sec. III) after each individual measurement. Note that the permittivity for the empty Vycor sample varied only slightly between two measurements, indicating a complete removal of the alcohols.

The results of these concurrent adsorption experiments as a function of $\sqrt{t}$ are shown as continuous lines in Figs. 8(a)–8(e). Two regions of different dynamics become apparent. The first region only contains contributions from vapor adsorption, since liquid influx is at first limited to the bottom of the sample [see Fig. 8(f)]. As the imbibition front advances from the bottom face, it passes the bottom edge of the electrode at a certain time [see Fig. 8(g)]. After that, the superposition of both capillary dynamics and adsorption dynamics can be seen, similar to imbibition experiments. The resulting measurement then should reproduce the linearity from imbibition experiments, with an uncertainty whether the preadsorbed liquid changes the overall dynamics. Because of front broadening and the electrode stray field effects, the transition of both regimes is gradual, as indicated by the dotted lines in Fig. 8(d). It is worth noting that the filling fraction reached at the transition between both regions is in the order of $f = 0.2$, showing that the vapor phase has significant impact on the filling process.

During spontaneous liquid uptake, the presence of filled pores with concave menisci as additional adsorption spots

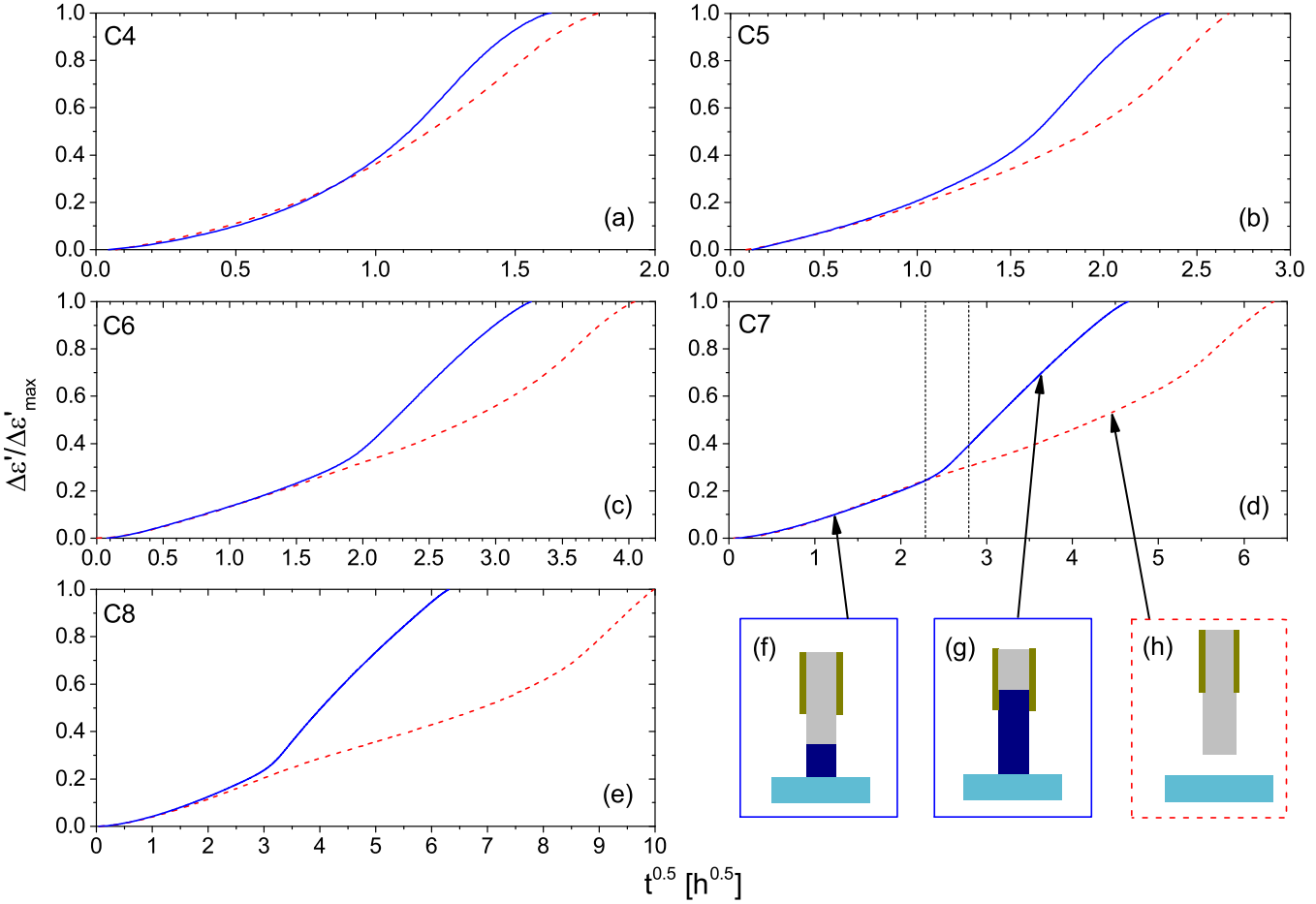


FIG. 8. Experimental results on vapor adsorption. (a)–(e) Comparison of "free" (dashed line) and "concurrent" (continuous line) adsorption experiments for $n$-alcohols ($n = 4$–8). Note that both curves show a good match at small times for all alcohols. (f) For concurrent vapor adsorption, the sample is only partially coated with electrode material and in contact with the liquid, inducing spontaneous imbibition. The measured filling curves then show two different regions: First, adsorbed vapor is detected. (g) After the imbibition front passes the electrode, vapor adsorption and imbibition both contribute to total filling. (h) During free adsorption, the same sample and electrode geometry is subjected to vapor adsorption only, there is no physical contact to the liquid surface (distance not drawn to scale).

could potentially influence diffusion dynamics in a macroscopic part of the sample. In order to gain insight into the magnitude of this effect, "free" adsorption experiments were performed on the same sample and electrode configuration [see Fig. 8(h)]. Here, the nanoporous matrix is suspended in vapor without contact to the liquid interface. Then, over the whole course of the experiment, the only filling mechanism is diffusion and adsorption through the vapor phase. The results are depicted as dashed lines in Figs. 8(a)–8(e).

A comparison of both concurrent and free vapor adsorption for the short-chain $n$-alcohols ($n = 4$–8) reveals good agreement of both experiments up to the point when the imbibition front reaches the electrode boundary. Thus, any long-range effects of the imbibition front on adsorption and diffusion dynamics can be ruled out, including a significant contribution of evaporation and recondensation from the advancing menisci. After that, the measured curves deviate from one another, as expected. However, for the smallest, most volatile molecules, complete filling in both experiments is achieved at comparable times. Again, this backs the hypothesis that vapor adsorption and diffusion is an important contribution to total filling dynamics for volatile liquids. In contrast, for longer chain lengths, the filling times for both methods differ considerably, which is why the additional uptake of molecules through vapor adsorption flux is not that prominent for liquids with lower vapor pressures.

A plot of free adsorption data as a function of $t$ allows further qualitative analysis of diffusion dynamics (see Fig. 9). In this diagram, the slopes are proportional to total diffusion flux into the sample. Changes in diffusion flux, according to Fick's first law, correspond to either a change in diffusivity, a change in the concentration gradient, or both. From theoretical considerations in Sec. II B, the concentration gradient inside the nanopores is at its maximum value for empty pores and decreases gradually for layer adsorption. During capillary condensation, the local vapor pressure at the menisci remains quasiconstant [see Eq. (4)], which translates to a constant concentration gradient as long as there are no critical changes in network topology. From NMR measurements, it is known that the diffusivity during adsorption changes continuously and approaches its minimum once capillary condensation starts [29]. In our free adsorption experiments, as depicted

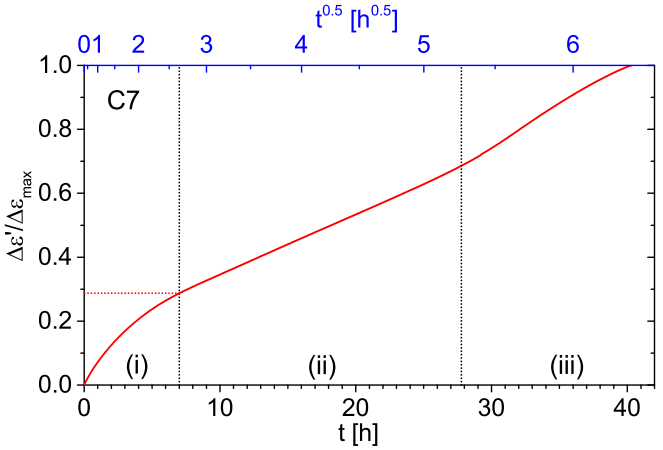


FIG. 9. Free adsorption dynamics, here for 1-heptanol (C7) [dashed line in Fig. 8(d)], as a function of $t$. Here, three stages with different dynamics can be defined. After an initial step (i), a stage with constant slope (ii) is found that extends over large periods of time. The final stage (iii) with Lucas-Washburn dynamics shows also as a linear segment of the dashed lines in Fig. 8 for large times.

in Fig. 9, we typically observe an initial step in filling (i), followed by a long linear segment (ii) and a final stage (iii) exhibiting $\sqrt{t}$ dynamics [also see the dashed line for large times in Fig. 8(d)]. Stage (i) qualitatively reflects the expectations from theory: The maximum diffusion flow is given for empty pores, then it decreases in agreement with changes in diffusivity and concentration gradient. The constant flux in stage (ii) is consistent with a constant concentration gradient to capillary bridges that do not significantly alter the pore network after their formation. The experimental data does not allow us to localize capillary bridges or to detect spatial rearrangements of the adsorbate. Due to the pore size distribution in Vycor, the first formation of capillary bridges is expected inside the smallest pores that are distributed all over the entire porous volume. The transition from (i) to (ii) is completed at $f \approx 0.28$ for heptanol, which is in good agreement to the amount of adsorbate at the onset of capillary condensation in sorption isotherms [24]. Finally, in stage (iii) the total flow increases again and slopes $\frac{\partial f}{\partial \sqrt{t}}$ approach those from the concurrent experiments [compare both curves in Figs. 8(a)–8(e)]. The values for these slopes are comparable to experimental Lucas-Washburn coefficients derived from Fig. 6, which suggests that spontaneous capillary flow also contributes to the free adsorption filling kinetics, although there is no physical contact to the liquid. A possible explanation for this is that more and more capillary bridges form close to the sample surface, which enable a spontaneous filling on condensation that is indistinguishable from liquid flow. In order to explain why the slopes match a one-sided spontaneous imbibition process rather than an all-sided imbibition, further investigation of stage (iii) is needed. Irrespective of the detailed filling mechanisms involved, the constant bulk diffusivity may limit the overall adsorption rate, but it does not completely mask the diffusion kinetics in the pores. Instead, the varying transport properties of the pore network are apparent in vapor uptake curves. These are at least consistent with the qualitative predictions from Sec. II B. A further analysis of the experimental data would require a detailed knowledge of the various transport coefficients involved.

### C. Combined imbibition and vapor condensation

Finally, we can evaluate the quantitative impact of adsorption during spontaneous imbibition by an empirical approach. So far, the total rate of capillary filling during imbibition was interpreted as a Lucas-Washburn law. Assuming a noninteracting superposition of both capillary flow and adsorption, the expected pore loading at time $t$ equals the sum of capillary filling with theoretical Lucas-Washburn coefficients $f_{\mathrm{LW}}(t) = \frac{c_h}{h_0}\sqrt{t}$ and a weighted contribution from the adsorption filling $f_{\mathrm{ads}}(t)$ in the empty parts of the sample:

$$f(t) = f_{\mathrm{LW}}(t) + \int_0^t [1 - f_{\mathrm{LW}}(\tilde{t})]\frac{\partial f_{\mathrm{ads}}(\tilde{t})}{\partial \tilde{t}} d\tilde{t}. \qquad (11)$$

For now, the Lucas-Washburn coefficients $c_h$ are calculated for a no-slip boundary condition, i.e., the solid black line in Fig. 7. Since we noticed no significant difference in the adsorption dynamics for free and concurrent adsorption for small times, the free adsorption results [dashed curves in Figs. 8(a)–8(e)] can be used as estimates for $f_{\mathrm{ads}}(t)$ rather than the concurrent adsorption results. This allows one to extrapolate $f_{\mathrm{ads}}$ up to the times for which the imbibition experiments are complete. A third order polynomial fit in $\sqrt{t}$,

$$f_{\mathrm{ads}}(t) = \sum_{i=1}^{3} a_i \sqrt{t^i}, \qquad (12)$$

matches the experimental free adsorption curves. Combining Eqs. (12) and (11), we obtain a corrected theoretical filling:

$$f(t) = f_{\mathrm{ads}}(t) + f_{\mathrm{LW}}(t)\left(1 - \sum_{i=1}^{3} \frac{i}{i+1} a_i \sqrt{t^i}\right). \qquad (13)$$

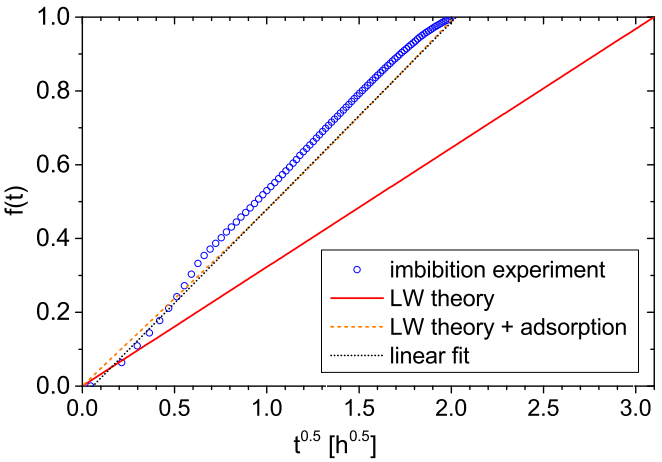


FIG. 10. Experimental normalized filling for pentanol ($n = 5$) (○) from imbibition experiments compared to Lucas-Washburn theory (continuous line) and to a superposition of capillary flow and (measured) adsorption from Eq. (13) (dashed line). A linear fit (dotted line) can be applied to the corrected theory in order to obtain corrected Lucas-Washburn coefficients $c_h$.

This corrected $f(t)$ is apparently not linear in $\sqrt{t}$. However, if higher order coefficients are sufficiently small, which is the case for the experimental adsorption rates, quasilinear regions emerge in plots for $f(\sqrt{t})$ (see the dashed line in Fig. 10). A fit has been applied so that the range in $\sqrt{t}$ matches phase (II) from imbibition experiments [see Fig. 6(b)]. The slopes of these fits can be used as corrected theoretical Lucas-Washburn prefactors $c_h'$, which are shown as the red dashed line in Fig. 7. With vapor adsorption included, an agreement to experimental data points is reached for small chain lengths, thus backing the hypothesis of a superposition of both adsorption and capillary flow.

## V. CONCLUSION

We have presented experimental data on liquid imbibition and vapor adsorption for $n$-alcohols in porous Vycor glass. While the simple Lucas-Washburn continuum model for capillary flow still is robust for long-chain alcohols with respect to the boundary condition, the experiments suggest that diffusion and adsorption from the surrounding vapor phase cannot be neglected in spontaneous filling if the liquids exhibit sufficiently high vapor pressures $p_0$. The adsorption dynamics, although impossible to calculate analytically, can be determined experimentally. A superposition of theoretical predictions for capillary flow rates and measured vapor adsorption explains our experimental findings for imbibition dynamics of $n$-alcohols with chain lengths $n \leqslant 8$. It is safe to say that in order to interpret any of these macroscopic experiments towards microscopic effects, e.g., slip-flow, one has to rule out any effects of vapor adsorption first.

Furthermore, it is shown that adsorption during imbibition behaves in the same way as adsorption for a sample only suspended in vapor, thus ruling out any significant long-range effects on adsorption kinetics because of liquid menisci at the imbibition front, including evaporation from the advancing imbibition front. The times for total filling by vapor adsorption are comparable to those for spontaneous imbibition for the shortest chain lengths and differ increasingly for lower vapor pressures. The adsorption dynamics for all alcohols can be split into three stages: The vapor uptake for small times can be identified as process of layer condensation. After that, over a large period of time, a constant diffusion flux $f \propto t$ is measured which is consistent with a nearly constant pressure gradient during capillary condensation. For large times, even without direct contact to the liquid, the adsorption rate can be described by a Lucas-Washburn law. We interpret this as a spontaneous capillary flow from capillary bridges close to the sample surface, which is indistinguishable from liquid uptake.

## ACKNOWLEDGMENTS

We thank B. Hallouet and E. Robert for their preliminary experiments as well as N. Bohr and J. Jacob for their work on testing and improving the experimental setup.

[1] P. Huber, J. Phys.: Condens. Matter **27**, 103102 (2015).
[2] M. S. Darsillo, H. D. Gafney, and M. S. Paquette, Inorg. Chem. **27**, 2815 (1988).
[3] T. Takahashi, Y. Yanagimoto, T. Matsuoka, and T. Kai, Microporous Mater. **6**, 189 (1996).
[4] F. Janowski, G. Fischer, W. Urbaniak, Z. Foltynowicz, and B. Marciniec, J. Chem. Technol. Biotechnol. **51**, 263 (1991).
[5] M. Sahimi, Rev. Mod. Phys. **65**, 1393 (1993).
[6] N. R. Morrow and G. Mason, Curr. Opin. Colloid Interface Sci. **6**, 321 (2001).
[7] W. H. Wade, Soc. Petr. Eng. J. **14**, 139 (1974).
[8] J. N. Israelachvili, J. Colloid Interface Sci. **110**, 263 (1986).
[9] C. Cheikh and G. Koper, Phys. Rev. Lett. **91**, 156102 (2003).
[10] W. Sparreboom, A. van den Berg, and J. C. T. Eijkel, New J. Phys. **12**, 015004 (2010).
[11] S. Gruener and P. Huber, Phys. Rev. Lett. **103**, 174501 (2009).
[12] S. Gruener, H. E. Hermes, B. Schillinger, S. U. Egelhaaf, and P. Huber, Colloids Surf., A **496**, 13 (2016).
[13] B. Smarsly, C. Göltner, M. Antonietti, W. Ruland, and E. Hoinkis, J. Phys. Chem. B **105**, 831 (2001).
[14] S. C. Reyes, J. H. Sinfelt, G. J. DeMartin, R. H. Ernst, and E. Iglesia, J. Phys. Chem. B **101**, 614 (1997).
[15] S. Gruener and P. Huber, Phys. Rev. Lett. **100**, 064502 (2008).
[16] M. Okazaki, H. Tamon, T. Hyodo, and R. Toei, AIChE J. **27**, 1035 (1981).
[17] R. Lucas, Kolloid Z. **23**, 15 (1918).
[18] E. W. Washburn, Phys. Rev. **17**, 273 (1921).
[19] M. Y. Lin, B. Abeles, J. S. Huang, H. E. Stasiewski, and Q. Zhang, Phys. Rev. B **46**, 10701 (1992).
[20] S. Gruener and P. Huber, J. Phys.: Condens. Matter **23**, 184109 (2011).
[21] Z. Sadjadi and H. Rieger, Phys. Rev. Lett. **110**, 144502 (2013).
[22] S. Gruener, Z. Sadjadi, H. E. Hermes, A. V. Kityk, K. Knorr, S. U. Egelhaaf, H. Rieger, and P. Huber, Proc. Natl. Acad. Sci. U.S.A. **109**, 10245 (2012).
[23] M. Alava, M. Dubé, and M. Rost, Adv. Phys. **53**, 83 (2004).
[24] D. Enke, F. Janowski, and W. Schwieger, Microporous Mesoporous Mater. **60**, 19 (2003).
[25] A. Mitropoulos, J. Colloid Interface Sci. **317**, 643 (2008).
[26] A. V. Neimark and P. I. Ravikovitch, Microporous Mesoporous Mater. **44-45**, 697 (2001).
[27] S. Chapman and T. G. Cowling, *The Mathematical Theory of Non-Uniform Gases: An Account of the Kinetic Theory of Viscosity, Thermal Conduction and Diffusion in Gases* (Cambridge University Press, Cambridge, England, 1970).
[28] M. Dvoyashkin, R. Valiullin, and J. Kärger, Phys. Rev. E **75**, 041202 (2007).
[29] R. Valiullin, S. Naumov, P. Galvosas, J. Kärger, H. Woo, F. Porcheron, and P. A. Monson, Nature (London) **443**, 965 (2006).
[30] P. Huber, S. Grüner, C. Schäfer, K. Knorr, and A. V. Kityk, Eur. Phys. J.: Spec. Top. **141**, 101 (2007).
[31] J. Kärger, D. M. Ruthven, and D. N. Theodorou, *Diffusion in Nanoporous Materials* (Wiley, New York, 2012), Vol. 1-2.
[32] T. Elmer, *Engineered Materials Handbook Volume 4: Ceramics and Glasses* (ASM International, Materials Park, OH, 1991), pp. 427–432.
[33] D. Argyris, N. R. Tummala, A. Striolo, and D. R. Cole, J. Phys. Chem. C **112**, 13587 (2008).

[34] G. P. Sinha and F. M. Aliev, Phys. Rev. E **58**, 2001 (1998).
[35] U. Kaatze, R. Behrends, and R. Pottel, J Non-Cryst. Solids **305**, 19 (2002).
[36] J. Dykyj, J. Svoboda, R. Wilhoit, M. Frenkel, and K. Hall, *Landolt-Börnstein - Group IV Physical Chemistry: Vapor Pressure of Chemicals—Vapor Pressure and Antoine Constants for Oxygen Containing Organic Compounds*, edited by K. R. Hall (Springer-Verlag, Berlin, 2000), Vol. IV/20B.
[37] C. Wohlfarth and B. Wohlfarth, *Landolt-Börnstein - Group IV Physical Chemistry: Surface Tension of Pure Liquids and Binary Liquid Mixtures*, edited by M. D. Lechner (Springer-Verlag, Berlin, 1997), Vol. IV/16.
[38] C. Wohlfarth and B. Wohlfarth, *Landolt-Börnstein - Group IV Physical Chemistry: Viscosity of Pure Organic Liquids and Binary Liquid Mixtures*, edited by M. Lechner (Springer-Verlag, Berlin, 2002), Vol. IV/20B.
[39] S. Gruener, T. Hofmann, D. Wallacher, A. V. Kityk, and P. Huber, Phys. Rev. E **79**, 067301 (2009).
[40] D.-S. Lee, Z. Sadjadi, and H. Rieger, Phys. Rev. E **90**, 013016 (2014).
[41] N. Asproulis, M. Kalweit, and D. Drikakis, Adv. Eng. Softw. **46**, 85 (2012).
[42] R. Pelster, Phys. Rev. B **59**, 9214 (1999).